Journal of Power Sources 187 (2009) 517–526

Contents lists available at ScienceDirect

Journal of Power Sources

journal homepage: www.elsevier.com/locate/jpowsour

Cold start dynamics and temperature sliding observer design of an automotive SOFC APU

Po-Hsu Lin, Che-Wun Hong*

Department of Power Mechanical Engineering, National Tsing Hua University, Hsinchu 30013, Taiwan

ARTICLE INFO

Article history:
Received 18 September 2008
Received in revised form 7 November 2008
Accepted 10 November 2008
Available online 21 November 2008

Keywords:
Solid oxide fuel cell
Auxiliary power unit
Sliding observer

ABSTRACT

This paper presents a dynamic model for studying the cold start dynamics and observer design of an auxiliary power unit (APU) for automotive applications. The APU is embedded with a solid oxide fuel cell (SOFC) stack which is a quiet and pollutant-free electric generator; however, it suffers from slow start problem from ambient conditions. The SOFC APU system equips with an after-burner to accelerate the start-up transient in this research. The combustion chamber burns the residual fuel (and air) left from the SOFC to raise the exhaust temperature to preheat the SOFC stack through an energy recovery unit. Since thermal effect is the dominant factor that influences the SOFC transient and steady performance, a nonlinear real-time sliding observer for stack temperature was implemented into the system dynamics to monitor the temperature variation for future controller design. The simulation results show that a 100 W APU system in this research takes about 2 min (in theory) for start-up without considering the thermal limitation of the cell fracture.

1. Introduction

Since more and more electronic devices are integrated into the vehicles as the standard equipment, the demand of electricity has approached to the limit of the current energy storage batteries. An independent power generation system with compact size and excellent efficiency is in need. Fuel cells are one of the solutions to current automotive designers. Delphi and BWM have developed a solid oxide fuel cell (SOFC) as an auxiliary power unit (APU) for transportation applications since 2000 [1–3]. The SOFC is a high temperature operation device with excellent thermal efficiency may exceed 50%. It can be fueled by the same diesel or gasoline used by the internal combustion engine, or even multi-fuel option, provided that an external reformer is installed. The tolerance of hydrogen impurity also makes the SOFC a suitable choice to be the automotive APU. However, the start-up for this kind of high temperature fuel cell from ambient is still a barrier for the automotive application. In this paper, the high temperature exhaust from a burner in the APU system was used to accelerate the heating up of the fuel, the air and the SOFC stack to reduce the cold start lag. A temperature sliding observer was designed to monitor the temperature variation of every important component based on some detectable system parameters.

2. SOFC APU system

Fig. 1 shows the schematic hardware design of the SOFC APU system in this research. Inputs of the SOFC are the compressed air and fuel (97% H_2 and 3% water vapor). The energy recovery unit (ERU) includes two plate heat exchangers to recover the thermal energy from the high temperature exhaust to preheat the inlet air and the inlet fuel of the SOFC stack. A controller was designed to regulate the valve flows via valve #1 and #2 in the diagram. In this paper, a dynamic model of the SOFC APU system was developed based on the mass and energy conservation laws in the system. The dynamic system model was coded on a Matlab/Simulink platform for on-line real-time simulation. A nonlinear sliding observer was then developed and embedded into the software SOFC system to carry out the temperature monitoring instantaneously. In this paper, the SOFC stack, the after -burner, the ERU and the nonlinear observer are the major subsystems. Their dynamics are described in the following sections.

2.1. Solid oxide fuel cell

Solid oxide fuel cells are one of the high temperature power generators. The high operating temperature enables the SOFC to achieve a high thermal efficiency with excellent tolerance of fuel impurity, comparing with other types of low temperature fuel cells. The SOFC model in this paper includes two dynamic systems: the electrochemical system and the thermo-fluid system. The former is a fast response reaction system, provided that the temperature is

* Corresponding author. Tel.: +886 3 5742591; fax: +886 3 5722840.
E-mail address: cwhong@pme.nthu.edu.tw (C.-W. Hong).

0378-7753/$ – see front matter © 2008 Elsevier B.V. All rights reserved.
doi:10.1016/j.jpowsour.2008.11.043

Nomenclature

A	area (m^2)
c_w	heat capacity of the wall ($kJ\,kg^{-1}\,K^{-1}$)
E	output voltage of solid oxide fuel cell (V)
E_{ideal}	ideal voltage of solid oxide fuel cell (V)
F	Faraday constant ($C\,mol^{-1}$)
F_T	correction factor of the heat exchanger
$\bar{f}$	range of parameter uncertainty
i	current density ($A\,cm^{-2}$)
i_0	exchange current density ($A\,cm^{-2}$)
i_{limit}	limiting current density ($A\,cm^{-2}$)
I	current demand (A)
h	enthalpy ($kJ\,kg^{-1}$)
h_0	stagnation enthalpy ($kJ\,kg^{-1}$)
N_c	number of the channels of the heat exchanger
n	number of transfer electrons
m	mass (kg)
k_1, k_2	sliding gain
P	pressure (kPa)
$\hat{P}$	estimated pressure (kPa)
Q	heat (J)
R	gas constant ($J\,mol^{-1}\,K^{-1}$)
R_{ohm}	fuel cell ohmic resistance (Ω)
S	entropy ($J\,K^{-1}$)
T	temperature (V)
$\hat{T}$	estimated temperature (K)
ΔT_{lm}	logarithmic mean temperature different
t	elapsed time (s)
u	specific internal energy ($kJ\,kg^{-1}$)
U	overall heat transfer coefficient

Greek letters

α	charge transfer coefficient
η_{act}	activation overpotential (V)
η_{con}	concentration overpotential (V)
η_{ohm}	ohmic overpotential (V)

Subscripts

HE	heat exchanger
amb	ambient
an	anode
ca	cathode
cold	cold
comb	combustion
g	gas
hot	hot
in	inlet
j	species of inlet gas
PEN	positive-electrolyte-negative
out	outlet
w	wall

raised to the operation criterion (800 K approximately). The latter is much slower because it involves the flow inertia and thermal inertia in the transport system, which consists of the pipes, valves, damping volumes, and heat exchangers in Fig. 1. The time lag of fluid dynamics and heat transfer among the flow transport is the major concern in the design of this fast start-up SOFC system.

The thermo-fluid system is modeled by a modified filling-and-emptying technique which was developed for the turbocharged engine simulation originally [4]. Both temperature and pressure dynamics are derived from the mass and the energy conservation laws plus the differential form of the gas state equation. The energy (temperature) and mass dynamics can be expressed by

$$\frac{dT}{dt} = \frac{\left(\sum(dQ/dt) + \sum_j h_{oj}(dm_j/dt) - u(dm/dt)\right)(1/m)}{\partial u/\partial T} \quad (1)$$

$$\frac{dm}{dt} = \sum_j \left(\frac{dm_j}{dt}\right) \quad (2)$$

where $\sum_j (dm_j/dt)$ is the summation of the mass that enters and leaves the control volume. The term $\sum(dQ/dt)$ includes all the heat transfer (through the control surface) and additional heat release (due to combustion or electrochemical reaction inside the control volume); $\sum_j h_{oj}(dm_j/dt)$ is the summation of the change of the specific stagnation enthalpy due to the mass flow in and flow out of the control volume; $u\,dm/dt$ is the internal energy variation due to the system mass change; $\partial u/\partial T$ is the specific heat at constant volume. The pressure dynamics inside the control volume can then be derived from the state equation of ideal gas, which takes the form of

$$\frac{dP}{dt} = P\left(\frac{1}{m}\frac{dm}{dt} + \frac{1}{T}\frac{dT}{dt}\right) \quad (3)$$

The electrochemical reaction rate is much faster than the flow of the thermo-fluid system. Hence, the output voltage of the electrochemical system of the SOFC can be evaluated quasi-statically and is expressed by

$$E = E_{ideal} - \eta_{act} - \eta_{con} - \eta_{ohm} \quad (4)$$

where E_{ideal} is the theoretical Nernst voltage of the SOFC; η_{act}, η_{con} and η_{ohm} are the activation overpotential, the concentration overpotential and the ohmic overpotential, respectively. These overpotentials are related with the operation current density, i, and the instantaneous stack temperature, T, as below

$$\eta_{act} = a + b\ln i \quad \text{where} \quad a \approx -\frac{RT}{n\alpha F}\ln i_o \ \text{ and } \ b \approx \frac{RT}{n\alpha F} \quad (5)$$

$$\eta_{com} = -\frac{RT}{nF}\ln\left(1 - \frac{i}{i_{\text{limit}}}\right) \quad (6)$$

$$\eta_{ohm} = I R_{ohm} \quad (7)$$

where a and b are the span and the slope of the Tafel plot of the activation overpotential; n is the number of transfer electrons; α is the charge transfer coefficient; F is the Faraday constant; R is the gas constant; T is the operation temperature; i_0 is the exchange current density; i_{limit} is the limiting current density; R_{ohm} is the total resistance of the electrolyte, and I is the current demand. All the terms in the right-hand-side of the above equations are functions of the stack temperature T, and temperature is a function of time in our case. Hence the first-order nonlinear differential equations in Eqs. (1–3) configure the system dynamics of the control volume. The SOFC stack temperatures, including the anode chamber temperature, cathode chamber temperature, and the electrolyte (or positive-electrolyte-negative, PEN) temperature, are the major parameters to be observed for control purposes [5,6].

An orifice analogy model to simulate the mass flow across the boundary due to pressure difference between control volumes has been employed. The mass flow rate is calculated by an isentropic

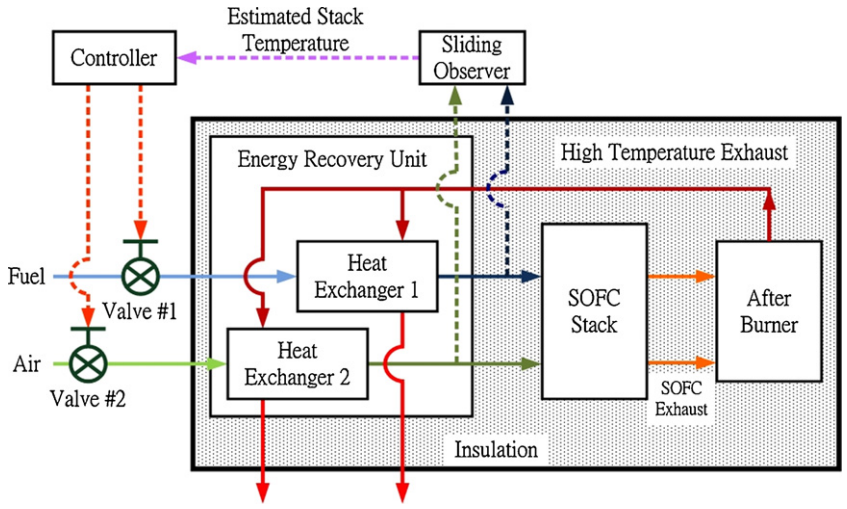

Fig. 1. Schematic of a typical SOFC APU system.

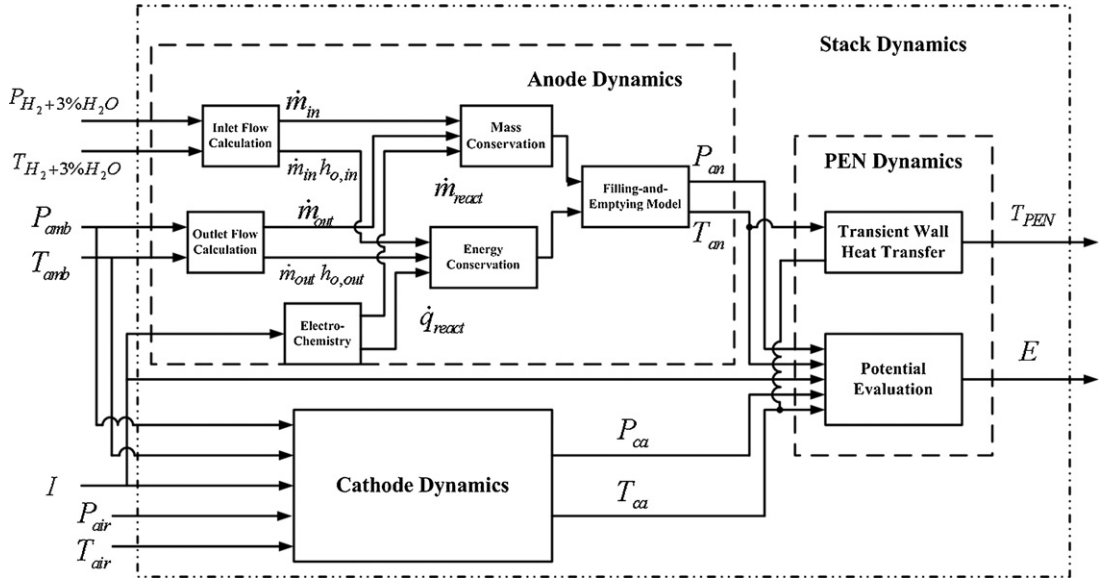

Fig. 2. Block diagram of the SOFC stack dynamics calculation.

nozzle flow multiplied by a discharge coefficient as

$$\frac{dm_j}{dt} = C_d A_b \frac{P_u}{\sqrt{T_u}} \sqrt{\frac{2\gamma}{R(\gamma-1)}} \sqrt{(P_r)^{2/\gamma} - (P_r)^{\gamma+1/\gamma}} \times \begin{cases} \text{if } \dfrac{P_d}{P_u} > \left(\dfrac{P_d}{P_u}\right)_{crit} = \left(\dfrac{2}{\gamma+1}\right)^{\gamma/\gamma-1} & \text{then } P_r = \dfrac{P_d}{P_u} \\ \text{if } \dfrac{P_d}{P_u} \le \left(\dfrac{P_d}{P_u}\right)_{crit} & \text{then } P_r = \left(\dfrac{P_d}{P_u}\right)_{crit} \end{cases} \tag{8}$$

where C_d is the discharge coefficient; A_b is the flow area at the boundary; P_u, P_d, P_r are the upstream, downstream pressures and the pressure ratio; T_u is the upstream temperature; R is the gas constant and γ is the specific heat ratio.

Fig. 2 shows the block diagram of the calculation of the SOFC stack dynamics. The SOFC model includes the blocks of the anode dynamics, the cathode dynamics and the PEN dynamics. The upper left side of the figure shows the detailed flow diagram of the calculation of the anode dynamics. The cathode dynamics resemble the anode dynamics. Note that the inputs of the whole block diagram are: P_{amb}, T_{amb}, P_{H_2}, T_{H_2}, P_{air}, P_{air} and the current demand I; the out-

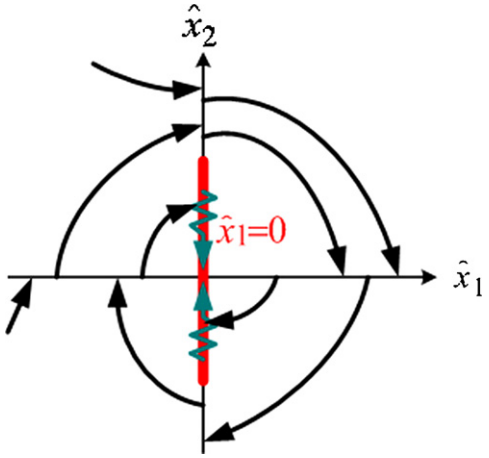

Fig. 3. Concept of the sliding surface.

Table 1
The specification and operating conditions of the SOFC APU system.

Component	Specification and operating conditions
Solid oxide fuel cell	Type: Co-flow planar SOFC Stack volume: 10 cm × 25 cm × 15 cm Single cell reaction area: 50 cm^2 Numbers of cells: 5 Suggested operation temperature: 1100 K Fuel: 97% hydrogen + 3% water vapor Input pressure: 150 kPa Input temperature: 300 K Oxidizer: air Input pressure: 180 kPa Input temperature: 300 K Rated power: 100 W
Heat exchanger	Plate type Channel numbers: 16 Heat transfer coefficient: 929 $Wm^{-2}K^{-1}$ Exchange area: 0.0729 m^2 Correction factor: 1

put variables ate the stack voltage E and the PEN temperature T_{PEN}. A 3% of water vapor is added into the H_2 inlet stream for protection purpose. The H_2 consumption rate can be estimated from the Faraday law, that is

$$\dot{m}_{H_2} = \frac{I M_{H_2}}{nF} \tag{9}$$

where I is the current demand from the external load; M is the molecular weight; n is the number of transfer electrons; F is the Faraday constant.

2.2. After-burner

An after-burner is placed at the exit of the SOFC stack to raise the exhaust gas temperature by burning the residual fuel. This high temperature exhaust gas is then fed back as the heat source for those two heat exchangers in the energy recovery unit. The burner is considered as an adiabatic system so that the heat released from combustion is totally utilized to increase the gas temperature. The temperature and the pressure dynamics of the burner are calculated from Eqs. (1) and (3). An additional term dQ_{comb}/dt was added in Eq. (1) to take account of the chemical energy release during combustion.

The combustion heat release rate is derived from the enthalpy change rate between the product (at product temperature T_p) and the reactants (at reactant temperature T_r). It is expressed by

$$\frac{dQ_{comb}}{dt} = \dot{m}_p[\Delta h^o_{f,p} + h_p(T_p) - h^0_p] - \sum_r \dot{m}_r[\Delta h^o_{f,r} + h_r(T_r) - h^0_r] \tag{10}$$

where $\dot{m}$ is the consumption (or production) rate, h is the enthalpy. Subscripts f, p, r denote formation, product (water vapor) and reactants (hydrogen and oxygen); superscript 0 means at standard condition (1 atm, 298 K). Note that an iteration process is required to predict the burnt (product) temperature and the heat release in the same time (as described by typical thermodynamics textbooks).

2.3. Energy recovery unit

The energy recovery unit (ERU) retrieves heat from the high temperature exhaust of the burner and transfers it to pre-heat the SOFC stack. It consists of two plate heat exchangers which are used to heat up the incoming fuel and the incoming air respectively. The heat transfer rate of the plate heat exchanger can be expressed by [7]

$$\frac{dQ_{HE}}{dt} = (N_C - 1)A_{HE}U F_T \Delta T_{lm} \tag{11}$$

where Q_{HE} is the heat transfer rate; N_C is the number of channels; A_{HE} is the effective heat exchange area; U is the overall heat transfer coefficient; F_T is its correction factor [8]; and ΔT_{lm} is the logarithmic mean temperature difference, which is defined by

$$\Delta T_{lm} = \frac{(T_{hot,in} - T_{cold.out}) - (T_{hot,out} - T_{cold,in})}{\ln[(T_{hot,in} - T_{cold.out})/(T_{hot,out} - T_{cold,in})]} \tag{12}$$

The above equations are used to evaluate the heat transfer rate and the outlet gas temperature at steady state operation.

2.4. Transient wall temperature evaluation

The transient wall temperature (such as the PEN temperature) is evaluated from a first-order heat transfer equation as below:

$$m_w c_w \frac{dT_w}{dt} = h_g A_w (T_g - T_w) \tag{13}$$

where m_w is the wall mass, c_w its heat capacity of the wall, h is the effective heat convection coefficient, A_w is the wall area, T_g is the heating gas temperature and T_w is the wall temperature. Under transient conditions, a change in the effective gas temperature does not result in an instantaneous change of the stack wall temperature due to thermal inertia of the system. The actual wall temperature at time step $n+1$ is

$$T_{w,n+1} = T_{w,n} + (T_{w,n+1,\tau=0} - T_{w,n})(1 - e^{-\Delta t/\tau}) \tag{14}$$

The thermal time constant τ is calculated from an electric circuit analogy by

$$\tau = \frac{x_w \rho_w c_w}{h_1 + \frac{1}{x_w/k_w + 1/h_2}} \tag{15}$$

Table 2
Numerical values for the simulation parameters.

Component	Parameter	Value
SOFC	Volume of the anode chamber (V_{an})	0.0002 m^3
	Volume of the cathode chamber (V_{an})	0.0002 m^3
	Mass of the electrolyte	0.0003 kg
	Heat capacity of the electrolyte	1000 $J kg^{-1} K^{-1}$
	Charge transfer coefficient (α)	0.3
	Exchange current density (i_0)	0.1 $A cm^{-2}$
	Limiting current density (i_{limit})	0.9 $A cm^{-2}$
	Ohmic resistance (R_{ohm})	0.01 Ω
After-burner	Volume of the burner (V_{burner})	0.002 m^3
Heat exchanger	Volume of the heat exchanger chamber (V_{HE})	0.002 m^3
	Sliding gains (k_1, k_2)	200, 20
Observer	Initial estimated pressure ($\hat{P}$)	111.46 kPa
	Initial estimated temperature ($\hat{T}$)	400 K

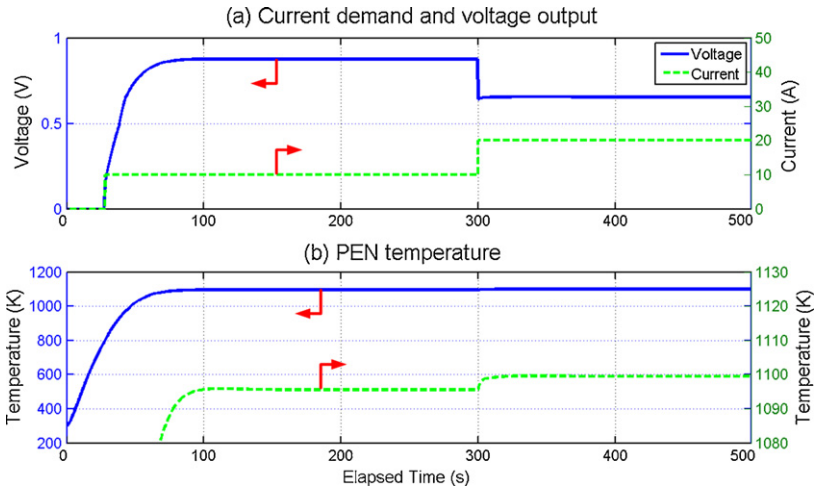

Fig. 4. Single cell voltage output, current demand and PEN temperature versus elapsed time showing the start-up and dynamic performance of the SOFC. (a) Current demand and voltage output, (b) PEN temperature.

in which, x_w is the wall thickness, ρ_w is the wall density, c_w is the specific heat capacity of the wall, k_w is the conduction coefficient of the wall, h_1 and h_2 are the heat convection coefficients of both sides of the wall.

2.5. Sliding observer

The SOFC stack is a high temperature operation device which needs to be thermally insulated in a chamber. The thermal effect plays the dominant factor that influences the SOFC performance. A novel sliding observer was designed to obtain the immeasurable gas temperatures inside the SOFC system via some measurable dynamic signals (such as pressure signals from the simulation). This is for future start-up control in the next research. Due to the fact that the system parameters are time dependent, the observer must be also a temporal function and possesses the robustness for parameter uncertainties. The sliding observer is designed based on a sliding surface concept, in which a switching law is added into the state dynamic equations of the whole system. The switching law is a function of the error between the target system state and the estimated system state. This observer shows sliding behavior in the estimated state trajectory as shown in Fig. 3. The sliding behavior enables the observer estimate the actual system state successfully in a short period even with a large model uncertainty and measurement disturbance [9–12].

In our case, we use the observer to acquire the system states that are difficult to be obtained in the realistic condition, such as the SOFC gas temperatures in the example system. The sliding observer for the anode dynamics is derived below as an example for the other parts of the SOFC APU system. The observer is built up to acquire the anode gas temperature based on available pressures whose equations are expressed by

$$\begin{aligned}\dot{\hat{P}}_{an} &= \hat{P}_{an}(d\hat{m}_{an}/(\hat{m}_{an}dt) + d\hat{T}_{an}/(\hat{T}_{an}dt)) + k_1 sgn(\tilde{P}_{an})\\ \dot{\hat{T}}_{an} &= \left[\left(\sum \frac{d\hat{Q}}{dt} + \sum_j \hat{h}_{oj}\frac{d\hat{m}_j}{dt} - \hat{u}\frac{d\hat{m}_{an}}{dt}\right)\frac{1}{\hat{m}_{an}}\right] / \frac{\partial \hat{u}_{an}}{\partial \hat{T}_{an}} + k_2 sgn(\tilde{P}_{an})\end{aligned} \tag{16}$$

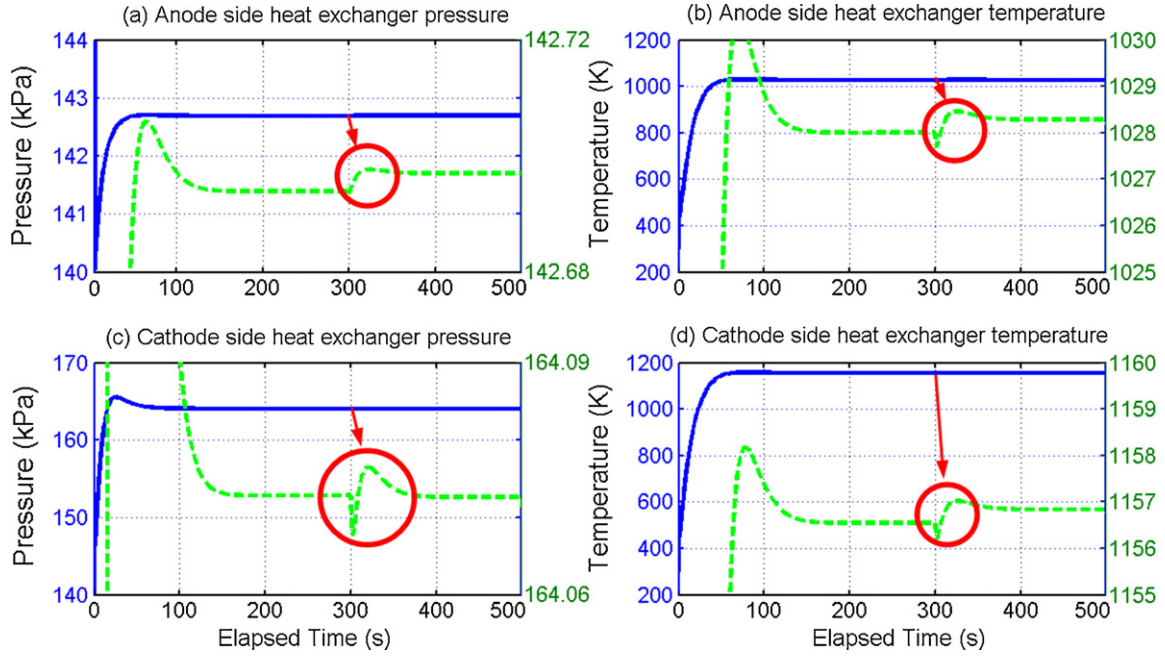

Fig. 5. Heat exchanger pressure and temperature dynamics of the fuel (anode side, (a) and (b)) and the air (cathode side, (c) and (d)) from start-up.

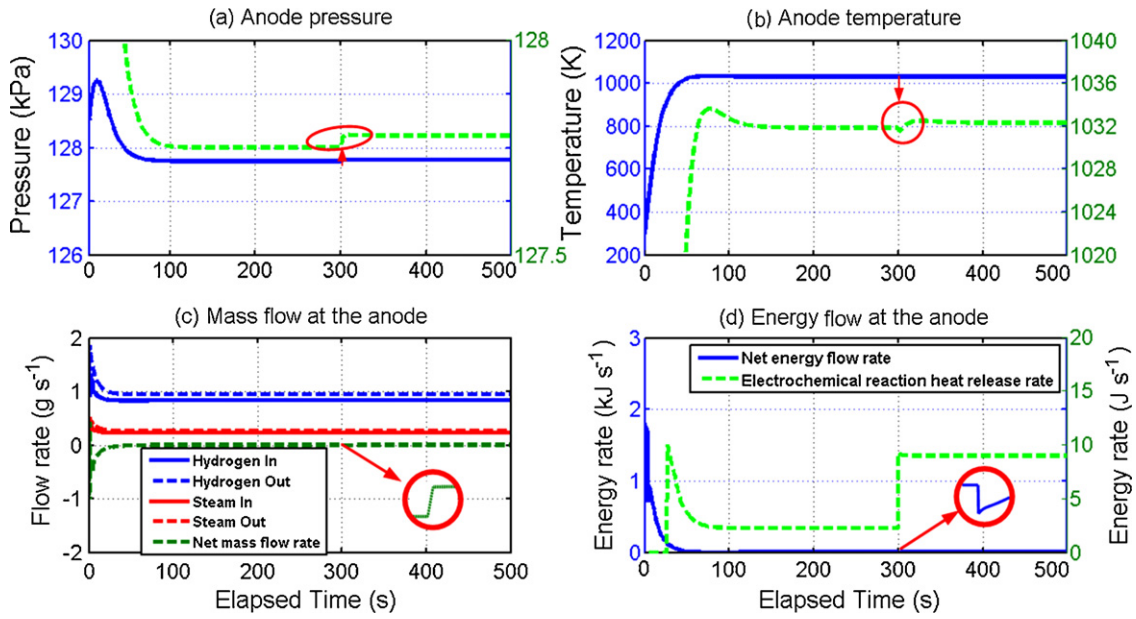

Fig. 6. Dynamics of the (a) pressure, (b) temperature, (c) mass and (d) energy flow of the anode volume.

where $\hat{p}_{an}$ and $\hat{T}_{an}$ are the estimated states; k_1 and k_2 are the sliding gains of the observer; $\tilde{p}_{an}$ is the error between the estimated pressure and the target pressure. The sliding states are set to be $\hat{x} = [\hat{x}_1 \quad \hat{x}_2] = [\hat{P}_{an} \quad \hat{T}_{an}]$, and the sliding surface is chosen as the pressure error ($\tilde{x}_1$) which is the difference between the estimated pressure and the target pressure:

$$s = x_1 - \hat{x}_1 = \tilde{x}_1 \tag{17}$$

and

$$\dot{\tilde{x}}_1 = \dot{x}_1 - \dot{\hat{x}}_1 = \Delta\dot{x}_1 - k_1 sgn(\tilde{x}_1) \tag{18}$$

The state trajectory will converge to $s = 0$, which means that the error $\tilde{x}_1$ will be zero, if the following equation is satisfied

$$\frac{1}{2}\frac{d}{dt}s^2 \le -\zeta sgn(s) \tag{19}$$

where ζ is a positive constant and sgn denotes 'sign', which is either positive or negative. If $\Delta\dot{x}_1$ in Eq. (16) is bounded by a constant $\bar{f}$, then the range of the sliding gain k_1 is

$$k_1 > \bar{f} + \zeta \tag{20}$$

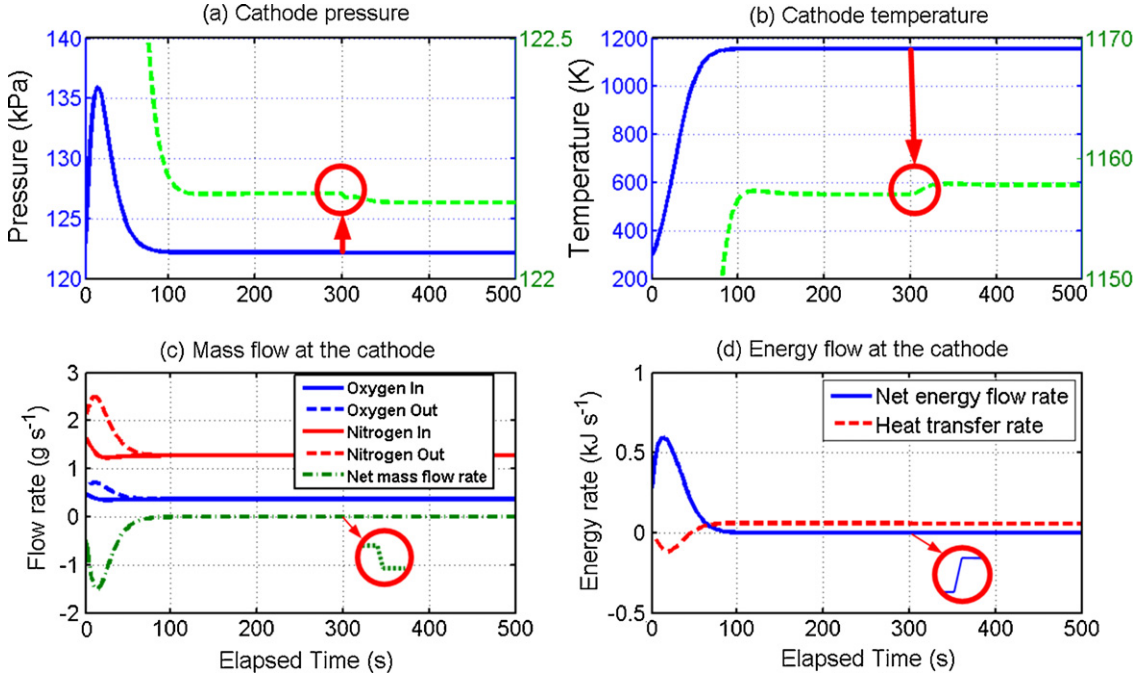

Fig. 7. Dynamics of the (a) pressure, (b) temperature, (c) mass and (d) energy of the cathode volume.

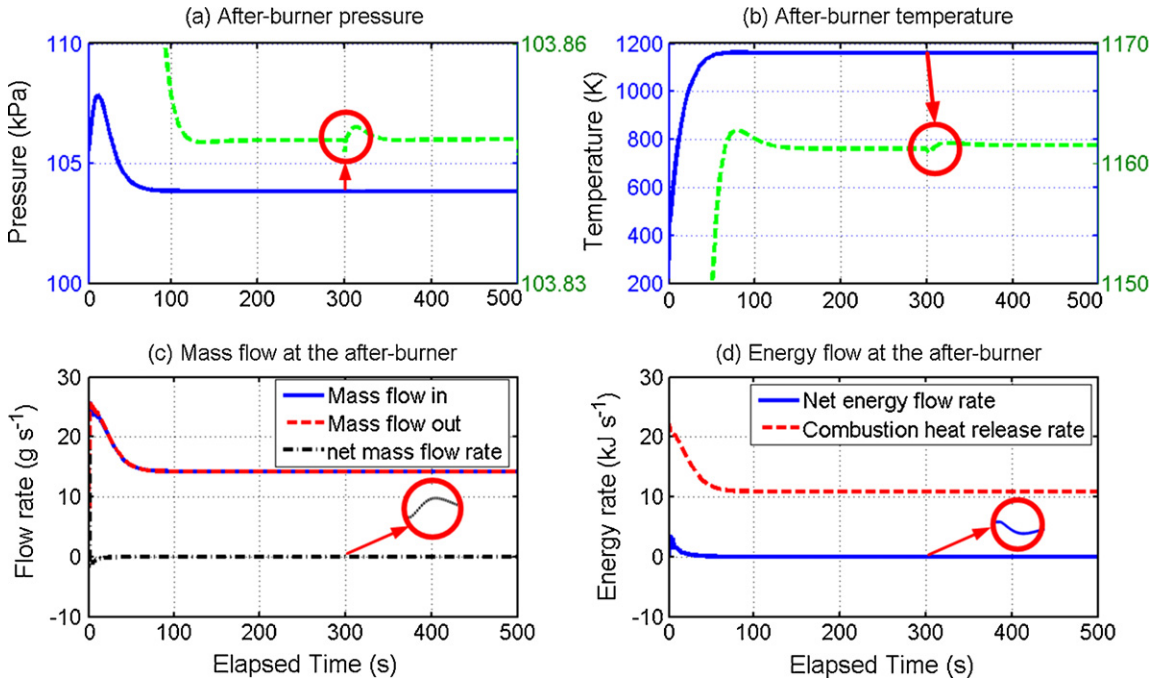

Fig. 8. Dynamics of the (a) pressure, (b) temperature, (c) mass and (d) energy of the after-burner.

A reduced dimensional sliding observer can be derived for $\dot{\hat{x}}_2$ from Eq. (15) that

$$\dot{\hat{x}}_2 = \frac{\partial(\Delta x_2)}{\partial \hat{x}_2} - \frac{k_2}{k_1}\frac{\partial(\Delta x_1)}{\partial \hat{x}_2} \equiv A_2 - B_2 C_2 \tag{21}$$

where A_2, B_2, C_2 are temporal variables and $A_2 = \partial(\Delta x_2)/\partial \hat{x}_2$, $B_2 = k_2/k_1$ and $C = \partial(\Delta x_1)/\partial \hat{x}_2$; Δx_2 is the difference between the target state x_2 and the estimated state $\hat{x}_2$. Eq. (21) will converge to zero if a proper sliding gain k_2 is selected. The sliding gain k_2 for the anode temperature observer can be obtained by the following equation:

$$k_2 = \frac{k_1 C_2(\beta - \alpha)}{A_2} \tag{22}$$

where α is the pole of A_2, and β is the new pole location. Similar procedure is applied to the cathode observer, and the representing PEN temperature is then calculated based on the estimated anode and cathode temperatures.

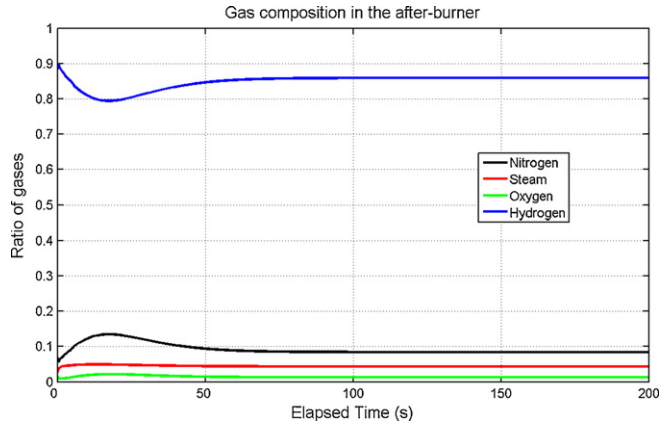

Fig. 9. Gas composition ratio variation inside the after-burner.

3. Simulation results

3.1. Transient performance under cold start condition

The dynamic models of each component of the SOFC APU system were built up and coded on a Matlab/Simulink platform. A numerical scheme ODE4 (Runge-Kutta) was employed to solve the three dynamic equations for mass, temperature and pressure respectively. The specification of the system, operating conditions and input numerical parameters are listed in Tables 1 and 2. The simulation was carried out on a typical Pentium 4 personal computer and the computation time is approximately half of the realistic operation time of the SOFC system.

Fig. 4(a) shows the current demand, single cell voltage output and the electrolyte temperature variation of the SOFC stack under a cold-start condition. Two stages of current demand were given: 10 A current was applied to the cell when the electrolyte temperature reached 800 K; 20 A was applied at the 300th second instantly to test the cell dynamics. In Fig. 4(a) and (b), the electrolyte temperature starts from 300 K and reaches 800 K at the 23rd second of the elapsed time. At this time a starting current 10 A is applied. The cell voltage in Fig. 4(a) increases with the stack temperature and keeps at a constant output at about 0.8 V. Fig. 4(b) shows the instantaneous PEN temperature and an enlarged view of the temperature variation is displayed below to trace all the transient conditions. The PEN temperature starts from 300 K and keeps at a constant temperature (about 1095 K) after 100 s. The magnified view reveals the relation between the temperature variation and the current command. The reason for the temperature variation is due to the heat released from the chemical reaction. The heat release becomes greater when a higher current demand is applied, so that the temperature climbs to a higher peak proportionally after 300 s.

Fig. 5 shows the pressure and temperature variation of the preheated hydrogen stream and air stream inside the energy recovery unit. The inlet pressures of both the hydrogen and the air are assumed to be 150 kPa and 180 kPa, respectively; the inlet temperatures are both set at the room temperature. The compressed

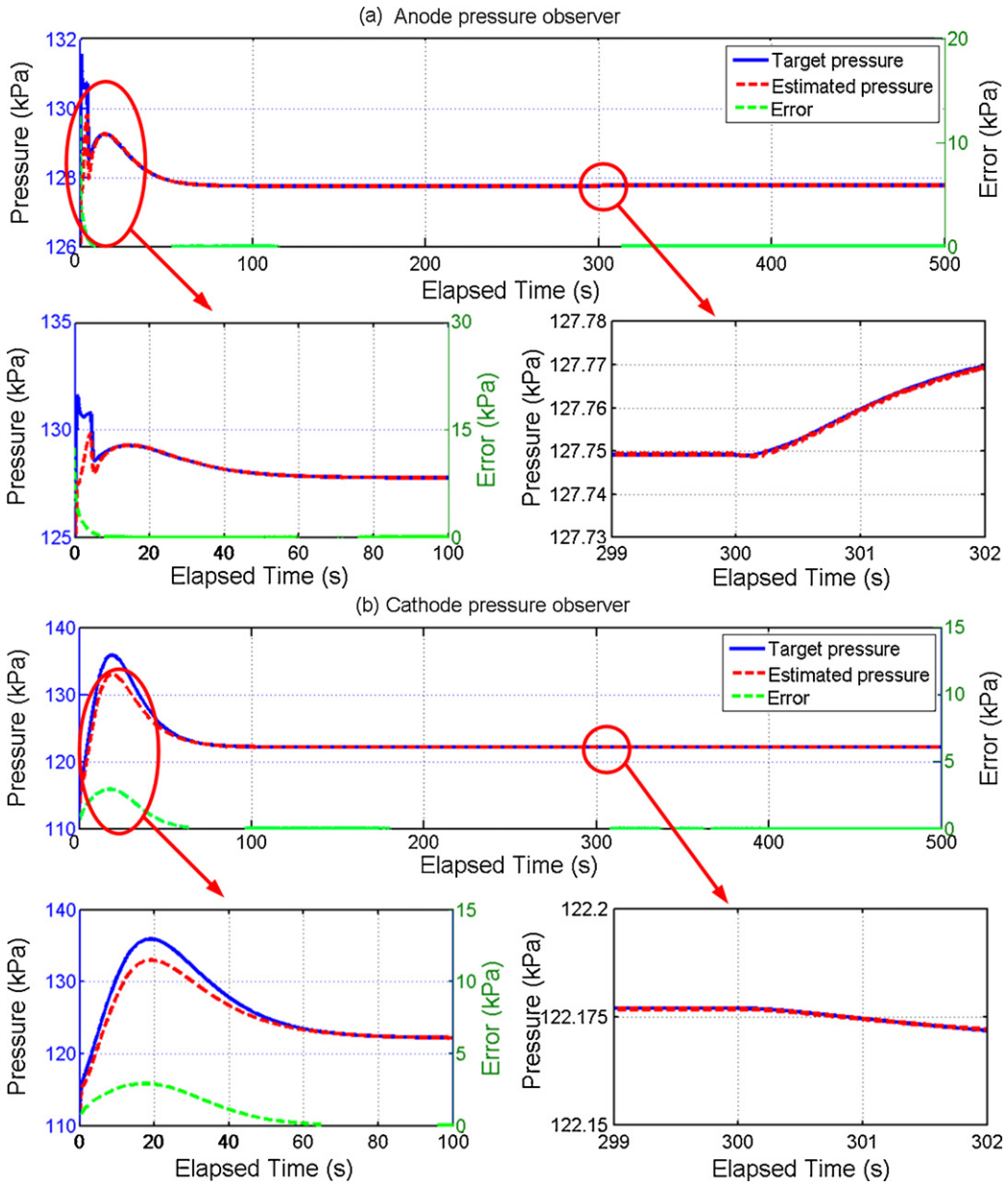

Fig. 10. Tracking performance of the sliding observer: (a) anode pressure; (b) cathode pressure. Enlarged views show the excellent tracking performance of the observer.

air is used to provide more oxygen to the SOFC and the burner. Fig. 5(a) and (c) show that the anode and cathode pressures vary at the beginning and then keep at a constant value near 142 kPa and 165 kPa after 100 s. They are both lower than the inlet pressure due to pressure drops across boundaries. Temperatures of the preheated fuel and the preheated air before entering the fuel cell increase with the burner temperature and reach to a constant value at about 1028 K and 1156 K, respectively. The preheated air temperature is higher than the fuel because of the difference of the heat capacity and the mass in the system. All the second peaks near the 300th second are due to the application of the current demand preset at 20 A.

The dynamics of the control volumes for the anode and the cathode plenums are shown in Figs. 6 and 7, respectively. Pressure variation in the beginning of the simulation can be observed in both anode and cathode volumes. This is due to the imbalance of the mass flow rate inside the channels as shown in Figs. 6(c) and 7(c). Note that when the anode pressure reaches steady state, the net mass flow rate of hydrogen and water vapor in the anode is still imbalance as shown in Fig. 6(c). This is due to an additional mass, oxygen ions, entered the anode plenum when the electrochemical reaction started, so that the mass flows out of the anode becomes higher in order to stabilize the pressure. In Figs. 6(b) and 7(b), both temperatures of the anode and the cathode rise from the beginning and stabilize at 1032 K and 1155 K, respectively. The anode temperature and the cathode temperature are higher than the input temperature because an additional heat release from the electrochemical reaction, i.e. $\left(\sum_i T_i \Delta S_i + I \sum \eta\right)$ in the energy equation. The values of the net energy flow, resulted from heat transfer, enthalpy flow in and out, internal energy change and the electrochemical heat release, are positive in Figs. 6(d) and 7(d). Hence, it raises the gas temperature in the control volumes.

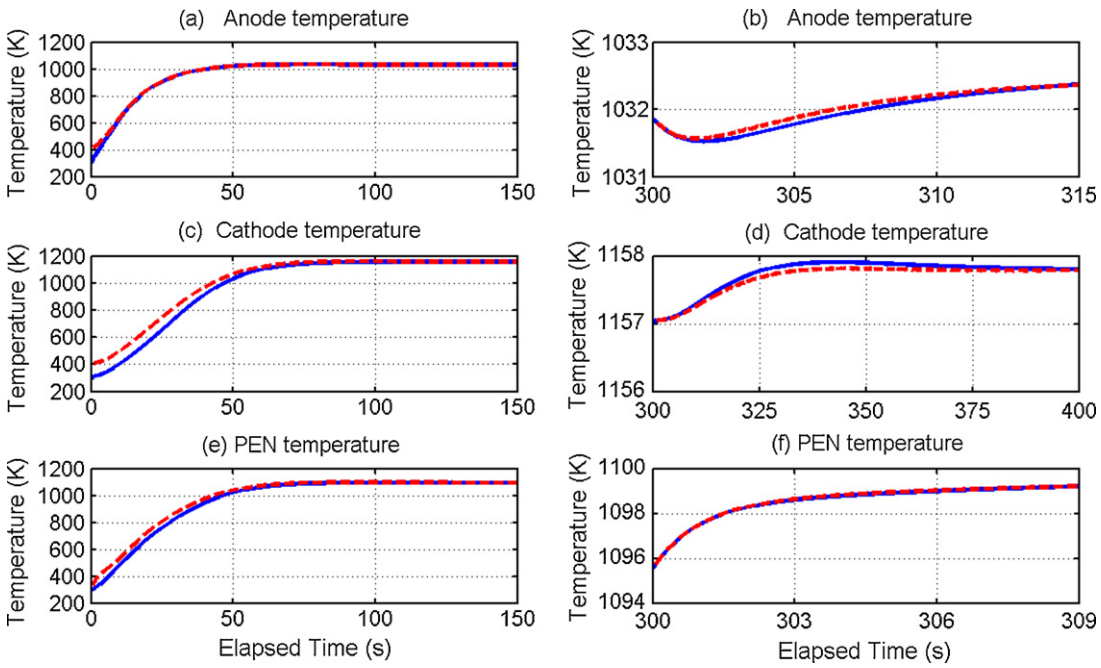

Fig. 11. Tracking performance of the sliding observer: (a) and (b) anode temperature; (c) and (d) cathode temperature; (e) and (f) PEN temperature. Magnified views show the estimated temperature (red dashed line) catches up the target temperature (solid blue line) before 100 s (within 2 min). (For interpretation of the references to color in this figure legend, the reader is referred to the web version of the article.)

The transient performance of the after-burner is shown in Fig. 8. The sudden increase of the pressure in the beginning, shown in Fig. 8(a), is due to the combustion heat release in Fig. 8(d). The burner pressure stabilizes at a constant value near 104 kPa after 100 s. The increase of the burner temperature in Fig. 8(b) is also due to the combustion heat release, and the temperature reaches 1160 K after the burner is ignited. Fig. 8(c) shows that the mass flow in and out of the burner balances all the time, except in the beginning, which means that the mass flow in an open system. In Fig. 8(d), combustion heat release results in the high temperature exhaust gas at the burner exit. Fig. 9 shows the gas composition variation inside the burner. During the unsteady combustion period, the ratio of the hydrogen drops from 0.88 to 0.79 and then returns to 0.86. Due to the drop of the hydrogen ratio, the other gas compositions slightly increase and then stabilize at a higher value than the initial condition after 100 s.

3.2. Tracking performance of the sliding observer

Fig. 10 shows the target pressure (solid blue), the estimated pressure (dashed red) and the estimation error (dashed green) of the anode observer and the cathode observer. In Fig. 10(a), the anode observer successfully tracks the target pressure after 10 s. The magnified view for the error shows that there is a peak which is about 20 kPa appearing in the beginning of the estimation and then chatters around zero during all the other transients in the later stage. Fig. 10(b) shows that the cathode observer successfully tracks the target pressure and reduces the error from 12 kPa to zero in 70 s. All the other transients are also well-predicted.

Fig. 11 shows the tracking performance of the temperature observer at the anode, the cathode and the PEN. The initial temperature for the observer was set at 400 K to magnify the effect of uncertainty, while the actual temperature starts from 300 K. Fig. 11(a), (c), and (e) indicate that the sliding observer (dashed red) tracks the actual temperature (solid blue) successfully in 60 s. Fig. 11(b), (d), and (f) reveal that the observed anode temperature, the cathode temperature, and the PEN temperature take approximately 10, 75, and 3 s to track back the original profile due to the sudden increase of the current at the 300th second. All the above results prove that the sliding observer is capable of feeding back a correct temperature to the SOFC controller which is still under development.

4. Conclusions

Cold start dynamics of a 100 W SOFC APU system have been investigated in this paper. A modified filling-and-emptying model was employed to derive the dynamic models of the SOFC system based on the mass and energy conservation laws. The high temperature exhaust of the embedded burner was used to accelerate the cold start of the APU system with an energy recovery unit. The simulation results show that the APU system temperature in this research takes 100 s in theory (without considering the material thermal stress problem) to reach the steady state. A nonlinear sliding observer was designed to obtain the immeasurable gas temperature instantaneously of the anode, the cathode and the electrolyte. The temperature observer is able to acquire the accurate state value in a short period with a proper sliding gain. It can be concluded at this stage that the observer is useful in developing a fast start-up controller for the APU system. A controller using the feedback observer temperature to track the gradient of the assigned heating up profile to avoid the fracture problem is under development.

Acknowledgments

The authors would like to thank the National Science Council (Taiwan) for financially supporting this research under contracts no. of NSC96-2221-E-007-061.

References

[1] J. Zizelman, J. Botti, J. Tachtler, W. Strobl, Convergence 2000-Paper 2000-01-C070, 2000.
[2] J. Zizelmanm, S. Shaffer, S. Mukerjee, SAE 2002-01-0411 (2002).

[3] C. Wunderlich, M. Boltze, 2005 Fuel Cell Seminar (2005).
[4] C.W. Hong, N. Watson, SAE Int. Congress and Exposition, SAE880122 (1988).
[5] C.H. Cheng, Y.W. Chang, C.W. Hong, ASME J. Fuel Cell Sci. Technol. 2 (2005) 219–225.
[6] P.H. Lin, C.W. Hong, J. Power Sources 160 (2006) 1230–1241.
[7] J.A.W. Gut, R. Fernandes, J.M. Pinto, C.C. Tadini, Chem. Eng. Sci. 59 (2004) 4591–4600.
[8] W.M. Rohsenow, J.P. Hartnett, Y.I. Cho, Handbook of Heat Transfer, 3rd ed., McGraw-Hill, New York, 1998.
[9] J.-J.E. Slotine, J.K. Hedrick, E.A. Misawa, Trans. ASME, J. Dyn. Syst., Meas. Control 109 (1987) 245–252.
[10] E.A. Misawa, J.K. Hedrick, Trans. ASME, J. Dyn. Syst., Meas. Control 111 (1989) 344–352.
[11] G.B. Chen, S.S. Peng, H.P. Huang, Chem. Eng. Sci. 52 (1997) 787–805.
[12] J.H. Choi, E.A. Misawa, G.E. Toung, Trans. ASME, J. Dyn. Syst., Meas. Control 121 (1999) 255–260.